J Vis (2015) 18:595–609
DOI 10.1007/s12650-015-0273-2

REGULAR PAPER

Z. Trávníček · Z. Broučková · J. Kordík · T. Vít

Visualization of synthetic jet formation in air

Received: 11 June 2014 / Revised: 30 December 2014 / Accepted: 30 December 2014 / Published online: 12 March 2015
© The Visualization Society of Japan 2015

Abstract This experimental study deals with a round synthetic jet (SJ) issuing into quiescent surroundings. Flow visualization in air is used to identify different flow field regimes. Hot-wire anemometry and theoretical evaluations are used to quantify parameters in terms of the Reynolds (*Re*) and Stokes (*S*) numbers. To verify the theoretical evaluation, additional experiments were performed using the laser Doppler vibrometry. Four regimes of oscillatory suction and extrusion are distinguished and presented by means of a *Re*–*S* parameter map: (a) creeping flow without SJ formation, (b) SJ formation and propagation without vortex rollup, (c) SJ with vortex rollup, and (d) vortex structure breakdown, instability and transition to turbulence. Differences in the SJ regimes at low, moderate and high Stokes numbers are found. While all four (a–d) regimes are identified for lower ($S < 10$) and moderate ($S = 10$–30) Stokes numbers, the SJ formation process for higher *Re* and *S* is coupled with the laminar–turbulent transition. The results are reasonably consistent with those in the available literature.

Keywords Synthetic jet · Flow visualization · Hot-wire anemometry · Laser Doppler vibrometry

1 Introduction

A synthetic jet (SJ) is a fluid jet flow created during an oscillatory process of suction and blowing between an actuator cavity and the ambient atmosphere. It is synthesized from the individual "fluid puffs" emitting out of the actuator orifice—Smith and Glezer (1998). The flow in the orifice reverses in each period, and the time-mean mass flux through the nozzle is zero. A common expression, the zero-net-mass-flux jet, follows from this fact—see Cater and Soria (2002). A few years later, the term "oscillatory vorticity generator" was suggested by Yehoshua and Seifert (2006) as being more appropriate.

The SJ phenomenon has a long history, being first observed in the 1950s, and is associated with problems with acoustic streaming. The first SJ (in today's terminology) actuator was most likely a laboratory air-jet generator designed and used by Dauphinee (1957). The basic advantage of an SJ is in its simplicity; no blower or fluid supply piping is required. As a result, SJs began to be investigated all over the world in connection with the active controlling of thermal and flow fields, as described by Yassour et al. (1986) and Meier and Zhou (1991), respectively. The phenomenon has become quite popular since the end of the last century when the term "synthetic jet" was introduced by James et al. (1996). Since that time, experimental,

Z. Trávníček (✉) · Z. Broučková · J. Kordík
Institute of Thermomechanics, Academy of Sciences of the Czech Republic, v.v.i., Dolejskova 5,
182 00 Prague 8, Czech Republic
E-mail: tr@it.cas.cz

T. Vít
Department of Power Engineering Equipment, Technical University of Liberec, Liberec, Czech Republic

theoretical and numerical investigations have continued to be performed to better understand and characterize this phenomenon—Kral et al. (1997), Mallinson et al. (2001), Lee and Goldstein (2002), Glezer and Amitay (2002), Gallas et al. (2003), and Kordík and Trávníček (2013). The reasons for the continued research include various applications of active control such as jet vectoring (Pack and Seifert 2001; Smith and Glezer 2002; Tamburello and Amitay 2007), jet shaking (Trávníček et al. 2012b) and flow control for external (Chen and Beeler 2002; Mittal and Rampunggoon 2002; Amitay and Glezer 2002; Tensi et al. 2002) and internal (Ben Chiekh et al. 2003) aerodynamics. Other relevant fields to this topic are heat transfer (Trávníček and Tesař 2003; Kercher et al. 2003; Mahalingam et al. 2004; Gillespie et al. 2006; Arik 2007; Valiorgue et al. 2009; Chaudhari et al. 2010; Persoons et al. 2011; Timchenko et al. 2007; Lee et al. 2012a, b; Trávníček et al. 2012c) intended for the cooling of electronic components and turbine blades.

While the basic features of SJs are general in character, specific regimes appear that are the product of the particular arrangement and actuation level. For example, very complex SJ regimes result from the interaction of an SJ with the main flow, such as jet flow control (Pack and Seifert 2001; Smith and Glezer 2002; Tamburello and Amitay 2007; Trávníček et al. 2012b). Another problem, which was studied by Hong (2006), is the control of laminar separation by means of triggering at the Tollmien–Schlichting and Kelvin–Helmholtz instabilities. Timchenko et al. (2007) and Lee et al. (2012a, b) investigated laminar microchannel flows by means of numerical simulations and suggested that SJs can produce a so-called quasi-turbulent flow characteristic with the potential for cooling microchips. A related problem was experimentally studied using PLIF and PIV by Xia and Zhong (2012b) where fluid mixing between two laminar water streams in a channel was enhanced by a pair of lateral SJs. An experimental study by Persoons et al. (2011) focused on impinging axisymmetric SJs from the point of stagnation heat transfer. A recent study by the same team (McGuinn et al. 2013) investigated the fluid dynamics using the same setup. Depending on a dimensionless stroke length, four regimes describing SJ flow morphologies were identified in both studies (Persoons et al. 2011; McGuinn et al. 2013).

Synthetic jets issuing into quiescent surroundings comprise a basic arrangement and is very useful for describing the different regimes. Several experimental studies discussing SJ regimes (some of them utilizing visualization) can be found in the available literature. For example, Xia and Zhong (2012a) investigated an axisymmetric SJ issuing into quiescent surroundings using sugar solution and silicone oil at very low Reynolds numbers. They suggested a parameter map in terms of the Reynolds–Stokes numbers or alternatively the Reynolds number and the dimensionless stroke length. They were able to distinguish four flow field regimes in the parameter map. More recently, this task was studied numerically by the same team—see Xia et al. (2014). Smoke-wire visualization by Goodfellow et al. (2013) demonstrated the SJ features during the suction and extrusion (blowing, pump) strokes of the actuation cycle (performed in quiescent surroundings).

Another aspect of SJs is the formation threshold. It is a known fact that the extrusion stroke must be strong enough to create a synthetic jet. The formation criterion quantifies the necessary conditions to overcome this threshold. The available literature contains systematic experimental evaluations for Stokes numbers ranging from 6 to 158 (Holman et al. 2005; Shuster and Smith 2007; Smith and Swift 2003; Milanovic and Zaman 2005). A pivotal paper was written by Holman et al. (2005). Based on the slug flow model analysis, numerical simulations, and experimental investigations, a criterion equation was formulated for axisymmetric and two-dimensional SJs. A recent paper by Trávníček et al. (2012a) extends the Stokes number range to a value of 292. Another approach was published by Timchenko et al. (2004) and Zhou et al. (2009) proposing an extension of the formation criterion for low Stokes numbers based on a theoretical analysis and numerical simulations.

A motivation of this study is the authors' opinion that flow visualization can be a valuable starting point for investigating SJ regimes for a large range of parameters. The main goal is to turn attention to SJ behavior at moderate and low Stokes numbers. To quantify the SJ parameters, a hot-wire measurement is used for overwhelming majority of experiments, whereas a theoretical evaluation by Kordík et al. (2014) is used for velocities below the limits of the hot-wire anemometer. To verify the theoretical evaluation, the laser Doppler vibrometry (LDV) experiments are performed.

2 Parameters of synthetic jets

Assuming the slug flow model, the two characteristic length scales for an axisymmetric SJ are the output orifice diameter D and the "stroke length" $L_0 = U_0T$, where T is the time period ($T = 1/f$, where f is

frequency) and U_0 is the time-mean orifice velocity defined from the orifice centerline velocity at the axis ($r = 0$) (Smith and Glezer 1998; Trávníček et al. 2012a):

$$U_0 = \frac{1}{T}\int_0^{T_E} u_0(r = 0,\ t)\,\mathrm{d}t, \tag{1}$$

where T_E is the extrusion time [e.g., $T_E = T/2$ for a common sinusoidal waveform of $u_0(t)$], and u_0 is the velocity at the orifice exit ($r = 0$, $x = 0$, for coordinates see Fig. 1).

The definition of the stroke length L_0 is well connected to the flow field and the slug flow model because it is the length of the liquid column extruded from the cavity during the extrusion stroke of the actuation period. The dimensionless extrusion stroke length is defined as L_0/D.

However, SJ formation for a given geometry is determined by two arbitrary dimensionless parameters from the following groups: the dimensionless extrusion stroke length (or the Strouhal number), the Reynolds and Stokes numbers (L_0/D (or St), Re, and S, respectively). The parameters Re, S, and St can be defined by several alternative manners. Note that the present definitions are consistent with those defined in Holman et al. (2005) and Trávníček et al. (2012a). The Reynolds number is defined by the time-averaged orifice velocity during the extrusion stroke, which is $2U_0$ for the sinusoidal waveform of the velocity cycle in the orifice. Therefore, $Re = 2U_0D/\nu$, where ν is the kinematic viscosity. Another useful definition is based on the stroke length ($Re_L = U_0L_0/\nu$), which characterizes the total amount of circulation generated during the extrusion stroke of the cycle. This serves to characterize the strength of the vortex rollup (Xia and Zhong 2012a; Zhou et al. 2009).

The Strouhal number is defined in terms of the angular frequency $\omega = 2\pi f$ as $St = \omega D/(2U_0) = \pi\ D/L_0$. The Stokes number is defined as $S = \sqrt{Re\ St}$. This definition can be rewritten without any additional assumptions as $S = D\sqrt{2\pi f/\nu}$, implying an independence from the reference velocity. Therefore, an evaluation of the Stokes number can be more precise than an evaluation of the Reynolds number (the uncertainties are estimated in "Appendix A").

3 Experimental approach

3.1 Synthetic jet actuator

Figure 1 shows the geometry of the SJ actuator, including the coordinate system axes x and r. The cavity is made of polymethyl methacrylate (PMMA or Perspex) tube with a 5-mm-thick wall. The cavity diameter and length are 60 mm and 84.5 mm, respectively. Two sharp-edged nozzles are used for this study, and the orifice diameter and length are denoted as D and L_D, respectively. The first (larger) nozzle is used for higher Re and S numbers: $D = L_D = 5.0$ mm. The other (smaller) nozzle is intended for smaller Re and S numbers: $D = L_D = 1.5$ mm. The outlets of the nozzles to the surroundings are oriented upwards.

Note that the previous version of this study, which was presented by Trávníček et al. (2013), used a smaller nozzle with a higher L_D/D ratio, namely $L_D = 14.7$ mm and $D = 1.6$ mm. However, a lack of similarity for nozzles with various L_D/D ratios may complicate the explanation of the SJ regimes because of a flow development process existing in the longer nozzle. Therefore, both nozzles in the present study have identical L_D/D ratios of 1. The L_D/D effect was studied by means of visualization by Crook and Wood (2001), who concluded that an increase in L_D promotes a flow development process, causing the boundary-layer thickness to increase. Moreover, the L_D increase promotes the occurrence of a tail-like structure behind the vortex ring (Crook and Wood 2001).

The electrodynamically driven diaphragm with a diameter of $D_D = 62.6$ mm originates from a 3-inch loudspeaker (AuraSound NS3-193-8A with RMS and peak power capacities of 20 and 80 W, respectively). The loudspeaker is very useful for SJ experiments because its diaphragm is made of aluminum and is quite rigid—see Kordík and Trávníček (2013).

Experiments with the smaller nozzle ($D = 1.5$ mm) used a transparent PMMA confining tube with a diameter and a length of 60 mm and 100 mm, respectively (see position 4 in Fig. 1). There are two reasons for the use of the confining tube: a reduction in the natural disturbances originating from surroundings into the area downstream of the nozzle and facilitating flow visualization at smaller velocities by means of a water fog. This method is described in part 3.2. The ratio of the confinement and nozzle diameters is 37.5,

which is considered high enough to neglect the wall effects in SJ formation and propagation processes—Xia and Zhong (2012a).

The working fluid in this experiment is air at barometric pressure and at room temperature (17–23 °C). The actuator is driven by a sinusoidal current from a sweep/function generator (AGILENT 33210A). No amplifier was needed in this study. The tested frequencies ranged from 3–96 Hz. The true RMS alternating current, voltage and power are measured by an in-house built digital multi-meter with the accuracies of ±0.5, ±0.5, and ±1 %, respectively. The sampling frequency was 13 kHz.

3.2 Experimental methods

Two flow visualization methods are used in this study, depending on the jet flow velocity. The first method is the smoke-wire technique. The smoke wire is made from three resistance wires 0.1 mm in diameter that are uniformly twisted together to increase the surface and prolong the observation time. This disrupts the flow slightly, over only 20 % of the hydraulic diameter. The smoke wire is located horizontally across investigated jet axis and is coated with a liquid (Fog Fluid, DANTEC) before each test. The smoke is created from Joule heating with a direct current. White streaklines can be observed on a black background (see Trávníček and Tesař 2003; Trávníček et al. 2012a for more details). The white streaklines, which trace the airflow, are traditionally called "smoke", but are in fact filaments consisting of aerosol producing by condensation. The smoke-wire visualization, though a simple and versatile tool, is not applicable for very low velocities. This is because the "smoke" rises up by natural convection from the heated smoke wire. An auxiliary experiment in quiescent air without an SJ was performed to evaluate this rising velocity. For this purpose, a digital camera in a continual recording regime at 30 frames per second was used. The rising velocity was evaluated to be approximately 0.04–0.08 m/s. This velocity corresponds reasonably well with a conclusion by Watson and Sigurdson (2008), who evaluated a slightly smaller value of 0.03 m/s for a smoke wire in a uniform horizontal crossflow at a velocity of 0.7 m/s.

The second visualization method, which is useful for small SJ velocities, uses cold water fog produced by an ultrasonic piezoelectric nebulizer (Mini Nebler). The fog is blown from the nebulizer to the

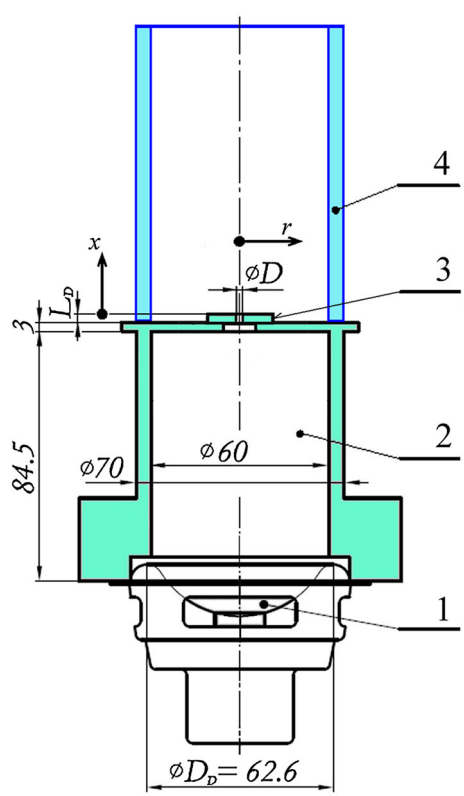

Fig. 1 Scheme of the investigated synthetic jet actuator; *1* loudspeaker, *2* cavity, *3* nozzle, *4* confining tube

surroundings of the SJ orifice. The fog is contained in the test section by the confining tube (position 4 in Fig. 1). After filling this tube with the fog from the open top, the fog is left to settle over a short period, typically 10–30 s. During this period, a boundary between the milky-looking fog and the clear ambient environment slowly descends. Finally, the SJ is turned on and visualization can be performed. An auxiliary experiment in quiescent air without an SJ was performed to evaluate the velocity of the falling fog. The settlement by a few centimeters was timed and the falling velocity was evaluated from repeated measurements to be approximately 0.001–0.002 m/s.

For both visualization methods, the phase-locked flow field patterns were observed under stroboscopic light (Cole Parmer 87002) synchronized with the excitation frequency at an arbitrary phase angle. Pictures were taken by a digital camera connected to a PC via a USB cable, using exposures ranging from 0.25 to 2.0 s. The resulting photo is a multi-exposure of a large number of frames (typically 10–100 frames), which shows the phase-locked feature of the flow field and smoothing out of the deviation fluctuations in the individual cycles.

An evaluation of the orifice velocity, and thus the Reynolds number quantification, was made by means of the two methods. The first method is a direct measurement of the flow velocity at the nozzle exit, u_0, using the hot-wire anemometry. The other method, which is useful for velocities below the limits of the hot-wire anemometer, is a theoretical evaluation of the oscillating diaphragm displacement, recently proposed and verified by Kordík et al. (2014).

A DANTEC MiniCTA 55T30 anemometer was used in constant temperature anemometry (CTA) mode with a single-sensor wire probe (55P16) with an NI PCI-6023E data acquisition device. The sampling frequency and the number of samples were 0.15–10 kHz and 32,768, respectively. For these experiments, the anemometer was calibrated over a velocity range of 0.2–37 m/s, and the linearization error of the calibration (using a four-degree polynomial) was within 8.6 %.

A triple decomposition process was used for the velocity analysis. The definition of the velocity components in the streamwise direction is $u = U + U_P + u'$, where u (t) is the instantaneous velocity, U, U_P (t/T) and u' (t/T) are the time mean, periodic (coherent), and fluctuating (incoherent, random) components, respectively, and t/T indicates the phase during the cycle. Velocity decomposition was based on continuous sampling at a chosen frequency. For the decomposition of the CTA data, the reference sinusoidal signal from the same sweep/function generator was acquired on the second channel, and phase averaging was performed according to the reference signal. The phase-averaged component and the root-mean-square value indicating u' were obtained during the cycle: $U + U_P$ (t/T) and u'_{RMS} (t/T), respectively. The number of the processed periods was on the order of 10^2. Considering the reciprocating velocity characteristics at the actuator orifice, positive (extrusion) and negative (suction) flow orientations were assumed and the velocities during the suction stroke were inverted to reflect the flow direction. The data processing procedure was scripted in MATLAB.

A CTA measurement at the SJ actuator orifice ($x = 0$, $r = 0$) was used to evaluate the velocity components $U + U_P$. Using Eq. (1), the time-mean orifice velocity, U_0, and the Reynolds number were evaluated. The relative uncertainties of the Reynolds numbers, based on a 95 % confidence level, were estimated within 17.2 and 10.7 % for experiments with nozzle diameters of $D = 1.5$ mm and $D = 5$ mm, respectively. More detailed information about the uncertainties estimation is available in "Appendix A".

A theoretical evaluation of the oscillating diaphragm displacement was made following the study by Kordík et al. (2014). The method is useful in the case of low Reynolds and Stokes number SJs when a direct measurement of the velocity u_0 at small-diameter nozzles can be problematic. This method was derived from the momentum equation of a mechanical oscillator and considers the electro-mechanical parameters of the specific electrodynamically driven loudspeaker-based actuator, such as the voice-coil resistance, inductance, force factor and the actuator diaphragm mass. Based on the measurements of the actuator electrical input (alternating current and voltage), the method yields the diaphragm velocity amplitude. Assuming continuity and fluid incompressibility for air as the working fluid, the velocity in the nozzle can be evaluated with a reasonable accuracy. An experimental validation of the method was performed using the hot-wire anemometry and laser Doppler vibrometry, which included the evaluation of the incompressibility criterion, comparison with the available literature, ranges of applicability, uncertainties and limits. For further information, see the paper by Kordík et al. (2014). For the parameters of the present study, the relative uncertainties of the Reynolds numbers based on the theoretical evaluation were within 18.3 and 10.1 % for nozzle diameters of $D = 1.5$ mm and $D = 5$ mm, respectively. The confidence level of the uncertainties is 95 % (see "Appendix A" for more details).

To validate the theoretical evaluations of the diaphragm displacement, diaphragm velocities were measured via laser Doppler vibrometry (LDV). A portable digital vibrometer (Ometron VH-1000-D, B&K 8338) was used. The laser beam was targeted through the SJA nozzle (for $D = 5$ mm) or through an auxiliary glass window (for $D = 1.5$ mm; the glass window is not depicted in Fig. 1) onto the center part of the diaphragm. The velocity of the oscillating diaphragm surface was measured during the driven cycle. The LDV signal was sampled in the data acquisition device (NI-PCI 6023E) at 16,384 samples and at a sample rate of 128*f*. For the decomposition of the LDV data, the reference signal from the same sweep/function generator was acquired on the second channel, while phase averaging was performed according to the reference signal. The procedure for data post-processing was developed in MATLAB.

The LDV data were used to evaluate the velocity at the orifice, u_0: Using the continuity equation, incompressible flow, the rigid (piston-like) diaphragm, and the slug flow model (i.e., uniform velocity profile issuing from the actuator orifice), the u_0 was evaluated. Integration according to Eq. (1) gives the time-mean orifice velocity U_0 for evaluation of the Reynolds number. Note that a similar method was used recently by Kordík et al. (2014). For the parameters of the present study, the relative uncertainties of the Reynolds numbers, based on a 95 % confidence level, were estimated within 8.7 and 7.8 % for experiments with nozzle diameters of $D = 1.5$ mm and $D = 5$ mm, respectively (see "Appendix A" for more details).

4 Results and discussion

4.1 Flow field regimes

Figures 2, 3, 4, 5 and 6 demonstrate typical flow visualization results. Figures 2 and 3 are made using the smoke-wire technique, whereas Figs. 4, 5 and 6 are made using water fog from the ultrasonic nebulizer. Parameters of these visualizations are summarized in Table 1, including the measured RMS actuator voltage, which is considered valuable when addressing the reproducibility of the experiments. As written in the text above, the flow field regime (for a given geometry and sinusoidal current driving) is determined by two independent parameters. The Stokes and Reynolds numbers are chosen in this study. The presentation in Figs. 2, 3, 4, 5 and 6 uses the same *S* for each of Figs. 2, 3, 4, 5 and 6 with stepwise increasing *Re* in a, b, c, d pictures. The *Re* is based on the time-mean orifice velocity, U_0. An evaluation of the U_0 was made using a hot-wire anemometry for overwhelming majority of cases, whereas a theoretical evaluation by Kordík et al. (2014) was used for velocities below the limits of the hot-wire anemometer. To verify the theoretical evaluation, additional experiments were performed using the laser Doppler vibrometry (LDV). Table 2 summarized a comparison of the theoretically evaluated time-mean orifice velocities, U_0, with an evaluation from the LDV experiments for cases Figs. 4a, 5a and 6a.

As discussed by Xia and Zhong (2012a), four different flow field regimes can be identified. In agreement with this fact, the present flow visualization identified these four distinguishable regimes. Typical examples of these regimes (labeled a–d), which represent many repeated visualizations, are shown in Figs. 2, 3, 4, 5 and 6 (the nomenclature of the regimes a–d corresponds with the nomenclature of Figs. 2, 3, 4, 5, 6a–d):

(a) *Creeping flow without SJ formation* Fluid oscillations exist in the actuator orifice, but the vortices are not propagated far from the orifice. During the suction stroke of the cycle, the vortices move back towards the actuator. No organized fluid motion is observed in the test section except a fluid oscillation at the orifice and a consequent diffusion process at its vicinity.

(b) *SJ formation and propagation without vortex rollup* The extrusion stroke generates a lamellae-like structure, which is caused by the extruded fluid layers pilling together—see, e.g., Fig. 2b. Another typical feature is a mushroom-like forefront in the extruded fluid (visualized as a jellyfish or umbrella-shaped structure), as shown in Figs. 4b, 5b and 6b. Note that all the photos are multi-exposures of many frames, namely 12, 24 and 48 frames in Figs. 4b, 5b, and 6b, respectively. Therefore, it is obvious that the range of a fluid extrusion is limited to the visualized mushroom-like area and the fluid extruded from the actuator never leaves this area to travel further downstream. Although fluid motion from the orifice is clearly visible, the mushroom-shaped jet is weak for further downstream propagation. Moreover, the behavior of the jet flow appears irregular and intermittent. The flow field deviates from an ideal symmetry pattern—despite symmetrical boundary conditions—see asymmetry patterns in Figs. 2b and 3b. Apparently, this behavior is linked with low Reynolds numbers—cf. smoke-wire visualization experiments by Crook and Wood (2001).

(c) *SJ with vortex rollup* Individual vortices are stronger and capable of propagating farther downstream. The strength of the process depends on the total amount of circulation produced during the extrusions stroke,

which is characterized by the Reynolds number Re_L—see Zhou et al. (2009) and Xia and Zhong (2012a). According to Xia and Zhong (2012a), vortex rollup can only be observed when $S > 5$, $Re > 60$ or $Re_L > 100$. The present experiments are consistent with these results. Note that a range of an SJ propagation is visible for relatively large distance, up to $x/D = 15$–20 (for $D = 5$ mm in Figs. 2c, 3c) or even to $x/D = 50$–60 (for $D = 1.5$ mm in Figs. 4c, 5c, 6c). Obviously, SJ at the end of this range deviates for an ideal symmetry pattern—the reason of the asymmetry patterns is the same as discussed in the regime (b) above.

(d) *Vortex structure breakdown, instability, and transition to turbulence* In fact, this is a very complex process, which could be itemized into several stages. According to Xia and Zhong (2012a), the jet instability occurs at $Re > 200$ or $Re_L > 500$. Again, the present experiments reasonably agree with their results. It should be noted here that Figs. 4d, 5d, and 6d seem to be rather vague, because details of SJ structure are not caught there. An obvious reason is a very large extrusion stroke length L_0/D, comparable or even larger than the observed area (namely, $L_0/D = 21$–85, see Table 1).

Obviously, the phenomenon of various SJ regimes is complex and, thus, some differences are seen when our results are compared with the results from the available literature. For example, the present visualization indicates SJ formation and propagation from $S = 1.17$, whereas recent literature concluded an impossibility of SJ occurrence for $S < 2$ (Zhou et al. 2009; Xia and Zhong 2012a). These differences are attributed mainly to geometric variances.

Note that the present qualification that distinguishes the a–d regimes can be essentially compressed for higher Stokes numbers ($S > 70$) when regimes b–c–d proceed under a great overlap. Therefore, the transition to turbulence can be used as the SJ formation criterion for large values of S. Following this, the SJ formation criterion for larger values of S can be evaluated by means of the power spectra density, which was proposed for a range of $S = 73$–292 by Trávníček et al. (2012a).

Another interesting phenomenon involves the secondary structures that trail behind the primary vortex rings. It is known that an increase in L_0/D causes an increase in the vortex ring circulation (Zhou et al. 2009; Xia and Zhong 2012a). This mechanism should be saturated at the threshold value $L_0/D = 4$, and further L_0/D increases should generate secondary structures, such as trailing jets or/and secondary vortices. These structures can be observed in Figs. 2d and 3d for moderate values of $S = 21.8$ and 31.0 (despite the rather small values of $L_0/D = 3.05$ and 3.24, respectively) and in Figs. 4d and 5d for low values of $S = 3.31$ and 4.68, respectively.

4.2 Interpretation of the results in *Re*–*S* parameter map

To summarize the discussed regimes, Fig. 7a, b shows the parameter maps for $D = 5.0$ mm and 1.5 mm, respectively. The relationship between Re and S is presented. Besides the experimental parameters, Fig. 7a, b suggests three demarcation lines in the a–d regimes, denoted as a–b, b–c, and c–d. These lines fit the present visualization results. First, all three demarcation lines are proposed for $D = 5.0$ mm and $S > 10$ in

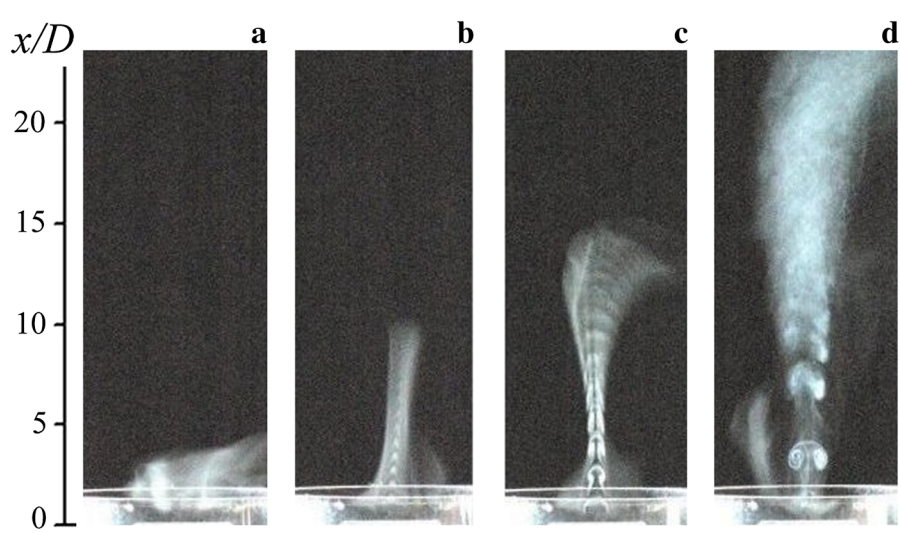

Fig. 2 Visualization at $S = 21.8$ with stepwise increasing $Re = 94$, 124, 201 and 464; parameters are summarized in Table 1

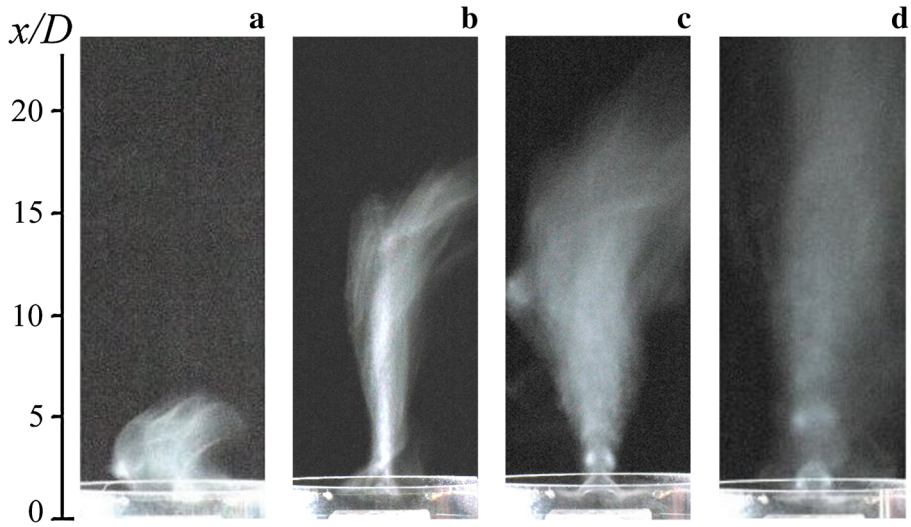

Fig. 3 Visualization at $S = 31.0$ with stepwise increasing $Re = 136$, 283, 580 and 993; parameters are summarized in Table 1

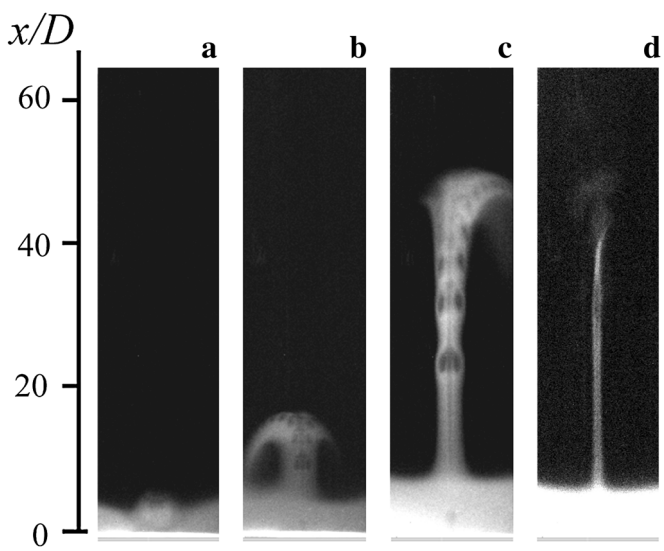

Fig. 4 Visualization at $S = 3.31$ with stepwise increasing $Re = 20$, 49, 103 and 295 (parameters—see Table 1)

Fig. 7a. For $S = 10$–25, lines a–b and b–c are close to approximately constant values of $Re_L = 50$ and 200, respectively. For higher values of $S = 25$–44, the lines a–b, b–c, and c–d are close to approximately constant values of $L_0/D = 0.7$, $L_0/D = 1.0$ and $Re_L = 650$. Note that line a–b quantifying the SJ formation threshold ($L_0/D = 0.7$) is reasonably close to the SJ formation criterion of $(L_0/D)_{crit} = 0.5$ as found by Holman et al. (2005).

Sequentially, the regimes demarcation lines are extended to lower values of $S < 10$, as shown in Fig. 7b. The dashed lines fit the present visualization results for $D = 1.5$ mm. For the sake of consistency, the full lines for $S > 10$ are replotted from Fig. 7a in Fig. 7b. A reasonable link-up of the full and dashed lines demonstrates experimental consistency and flow field similarity for nozzle diameters of $D = 5.0$ and 1.5 mm, respectively.

For comparison purposes, Fig. 7a, b shows the borders for the SJ formation and propagation without vortex rollup (dashed lines), SJ formation and propagation with vortex rollup (full lines) according to Zhou et al. (2009) and SJ thresholds for low Stokes numbers based on numerical simulations by Timchenko et al. (2004). Both these references were obtained by numerical simulations and resulted in much lower SJ thresholds than determined in the present result (line a–b). However, the present line b–c reasonably agrees

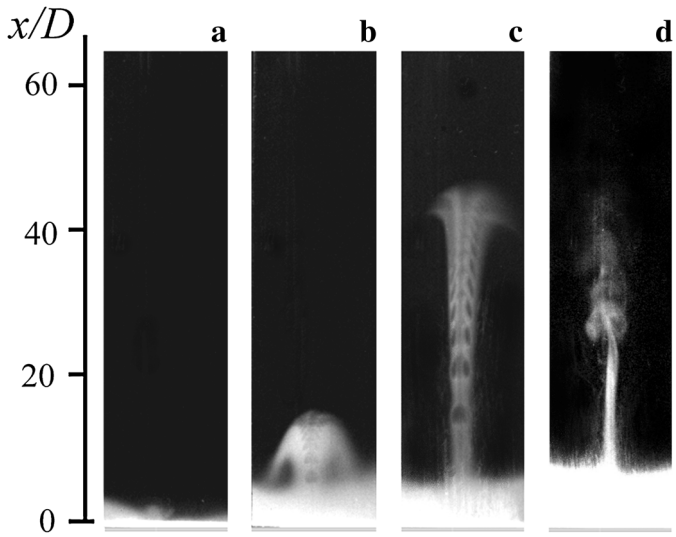

Fig. 5 Visualization at $S = 4.68$ with stepwise increasing $Re = 12$, 45, 99 and 330 (parameters—see Table 1)

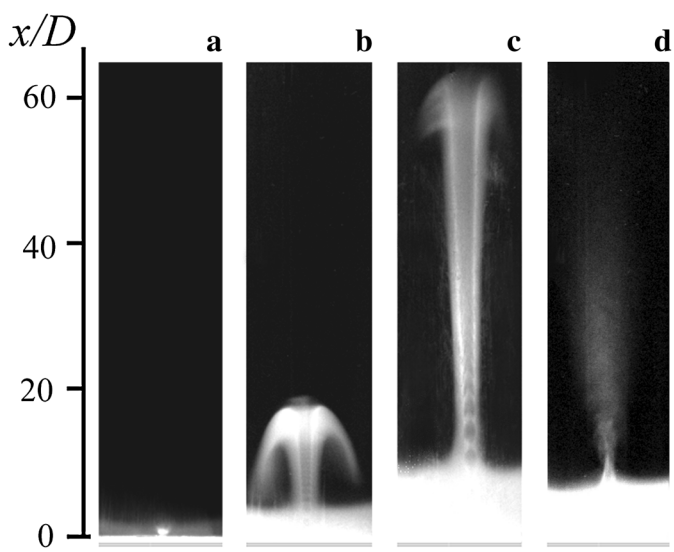

Fig. 6 Visualization at $S = 9.36$ with stepwise increasing $Re = 26$, 65, 139 and 595 (parameters—see Table 1)

with conclusions reached by Zhou et al. (2009) for $S > 8.5$. However, Zhou et al. (2009) did not identify the extension of line b–c for $S < 8.5$, whereas the present study extended line b–c towards a minimum value S of 1.7. Moreover, an available literature does not refer to SJs in regimes c and d for $S < 5.8$.

Figure 8 shows a comparison of the present results with the previous visualizations using a longer nozzle with dimensions $L_D = 14.7$ mm and $D = 1.6$ mm—Trávníček et al. (2013). As described, a longer nozzle promotes the flow development process, which is manifested in Fig. 8 by a systematic increase in the SJ formation threshold by 50–60 % (see the gray area between the dashed and dotted lines a–b in Fig. 8). However, the demarcation line b–c is nearly not influenced by the nozzle length variation. Finally, the demarcation line c–d was not identified for a longer nozzle in Trávníček et al. (2013). In other words, no vortex structure breakdown, instability, and transition due to turbulence were found for longer nozzles in Trávníček et al. (2013). It is believed that this laminarization effect is another consequence of the enhanced flow development process in the longer nozzle.

Moreover, Fig. 8 shows recent results of numerical simulations of SJs by Ng et al. (2013) performed for a longer nozzle of $L_D = 14.7$ mm and $D = 1.6$ mm [i.e., the longer nozzle according to Trávníček et al. (2013)]. Ng et al. (2013) obtained seven points of sustained SJs. Four points are very close to the present SJ

Table 1 Operating parameters of the present visualization experiments from Figs. 2, 3, 4, 5 and 6

Figures	Regime	D (mm)	f (Hz)	Voltage, RMS (mV)	U_0 (m/s)	L_0/D	Re	Re_L	S
2a	a	5.0	48.0	15.2	0.15	0.62	94	29	21.8
2b	b	5.0	48.0	22.6	0.19	0.81	124	50	21.8
2c	c	5.0	48.0	37.4	0.32	1.32	201	133	21.8
2d	d	5.0	48.0	95.5	0.73	3.05	464	708	21.8
3a	a	5.0	96.0	26.4	0.21	0.44	136	30	31.0
3b	b	5.0	96.0	56.2	0.44	0.92	283	130	31.0
3c	c	5.0	96.0	107.0	0.91	1.89	580	548	31.0
3d	d	5.0	96.0	202.0	1.55	3.24	993	1,609	31.0
4a	a	1.5	12.0	4.749	0.10	5.7	20	56.3	3.31
4b	b	1.5	12.0	9.550	0.25	13.9	49	337	3.31
4c	c	1.5	12.0	23.84	0.53	29.5	103	1,519	3.31
4d	d	1.5	12.0	96.06	1.52	84.6	295	12,479	3.31
5a	a	1.5	24.0	1.752	0.06	1.73	12	10.4	4.68
5b	b	1.5	24.0	5.321	0.23	6.5	45	147	4.68
5c	c	1.5	24.0	15.32	0.51	14.1	99	698	4.68
5d	d	1.5	24.0	97.52	1.70	47.0	330	7,755	4.68
6a	a	1.5	96.0	5.215	0.13	0.93	26	12.1	9.36
6b	b	1.5	96.0	10.67	0.33	2.3	65	74	9.36
6c	c	1.5	96.0	27.00	0.72	5.0	139	348	9.36
6d	d	1.5	96.0	236.7	3.07	21.3	595	6,337	9.36

Table 2 Comparison of the theoretical evaluation with an evaluation from the LDV experiments

Figures	U_0 evaluated from theory (m/s)	U_0 evaluated from LDV (m/s)	Relative difference (%)
4a	0.103	0.109	6.1
5a	0.062	0.072	16.2
6a	0.134	0.131	2.1

threshold line a–b. This was despite the fact that Ng et al. (2013) simulated a longer nozzle and line a–b was fitted to the present short nozzle of $L_D/D = 1$. Two points by Ng et al. (2013) are near the line b–c. Only one numerical point, $Re = 13.7$, is below the present region of the SJ. However, the SJ thresholds concluded from the numerical simulations by Timchenko et al. (2004) and by Zhou et al. (2009) indicated that this SJ threshold is best suited as the very minimum threshold (below the present experimental line a–b, as written in the text above).

The present parameter maps shown in Fig. 7a, b have been compared with recent experimental results by Xia and Zhong (2012a), as shown in Fig. 9. While the data from Xia and Zhong (2012a) for regimes c and d reasonably agree with the present results, the regime b at $S < 10$ occurs in Xia and Zhong (2012a) for one Re order of magnitude lower than the present data. The reasons may be the result of geometry differences. Obviously, the SJ threshold for low Stokes numbers is very sensitive to the geometry, setup and evaluation methods. It is fair to say that the present understanding of SJs at low Stokes numbers is far from complete.

Further specifications will be the matter of future investigations, based on various experimental methods. For example, two of the methods were successfully used by Trávníček et al. (2012a) for evaluation of the SJ formation threshold for large Stokes numbers, such as a rapid change in the power spectral density evaluated from the hot-wire data. Obviously, future experiments using optical methods such as PIV could better characterize the SJ flow fields and elucidate character of the demonstrated regimes—cf. PIV experiments focusing on the SJ formation criterion by Holman et al. (2005).

5 Conclusions

This visualization study addresses synthetic jets in air, focusing on the identification of flow field regimes. A quantification of the parameters was made using a hot-wire anemometry for overwhelming majority of experiments, whereas a theoretical evaluation by Kordík et al. (2014) was used for velocities below the limits of the hot-wire anemometer. To verify the theoretical evaluation, the laser Doppler vibrometry (LDV) experiments were performed.

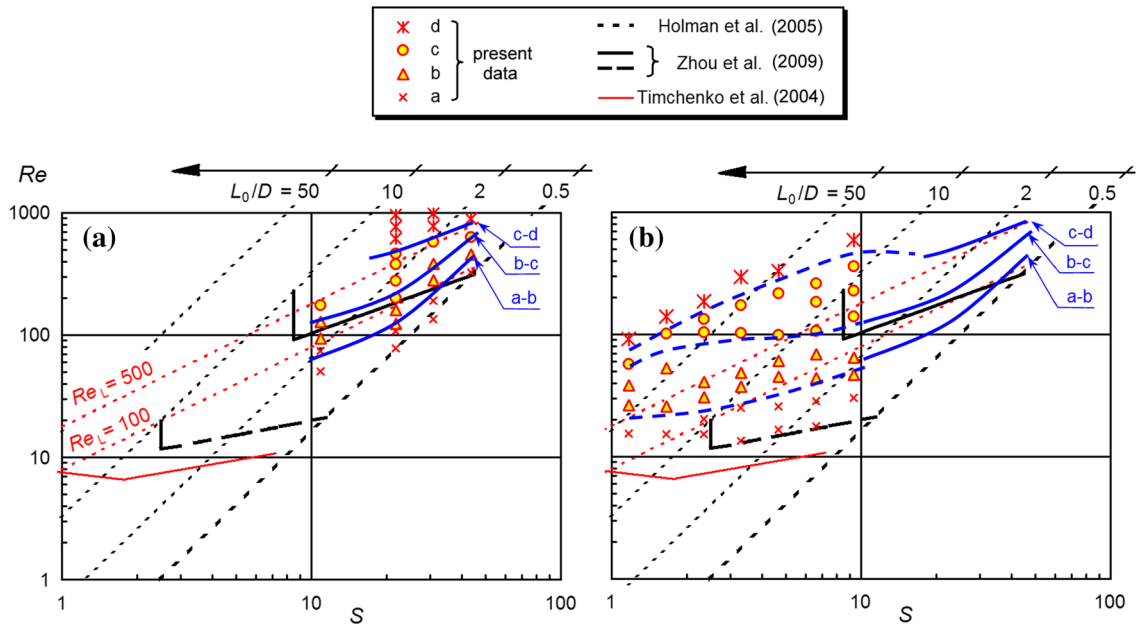

Fig. 7 Parameter maps with demarcation lines *a–b*, *b–c* and *c–d* based on the present data for nozzles with diameters of **a** $D = 5.0$ mm and **b** $D = 1.5$ mm

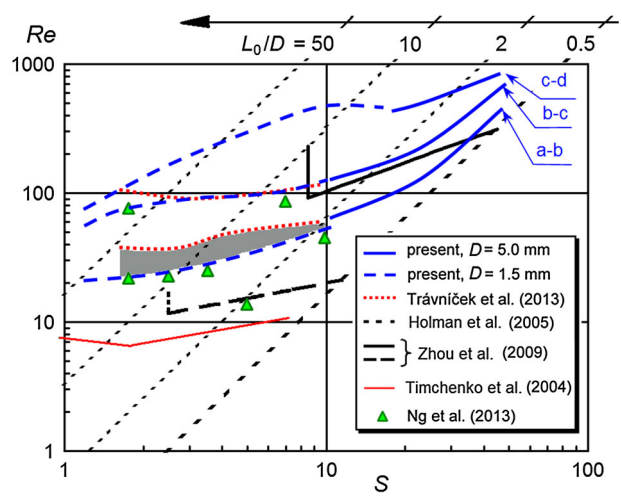

Fig. 8 Comparison of the present results (demarcation *lines* are proposed in Fig. 7a, b) with previous results for longer nozzle (Trávníček et al. 2013)—the differences are shown as the *gray color* area

In agreement with the literature, four different regimes for oscillatory suction and extrusion were distinguished: (a) creeping flow without SJ formation, (b) SJ formation and propagation without vortex rollup, (c) SJ with vortex rollup, and (d) vortex structure breakdown, instability and transition to turbulence.

The present experiments were conducted at the moderate/low Reynolds and Stokes numbers: $Re = 3.31$–$1{,}330$ and $S = 1.17$–44. All four regimes (a–d) were identified consistently using the available literature as references and displayed on a *Re–S* parameter map. Moreover, basic differences in the SJ regimes at low, moderate and high Stokes numbers were found. While all four regimes a–d can be distinguished at lower ($S < 10$) and moderate ($S = 10$–30) Stokes numbers, the SJ formation process for higher *Re* and *S* is coupled with the laminar-turbulent transition and overlaps in regimes b–c–d.

Future investigations can specify demarcation lines for regimes a–d on the proposed *Re–S* parameter map. For this reason, coupled experimental and numerical approaches are planned.

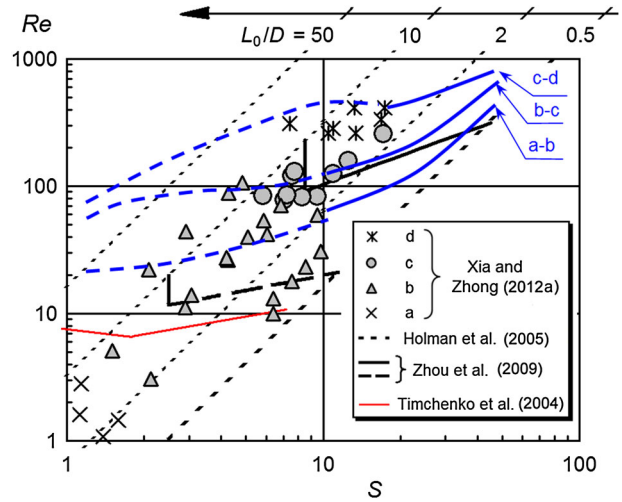

Fig. 9 Comparison of the present results (demarcation *lines* are proposed in Fig. 7a, b) with experimental data by Xia and Zhong (2012a)

Acknowledgments We gratefully acknowledge the support from the Grant Agency CR—the Czech Science Foundation (Project No. 14-08888S) and the institutional support RVO: 61388998.

Appendix A: Relative uncertainties of the Reynolds and Stokes numbers

Uncertainty analysis was performed according to the guidelines of BIMP et al. (2008).

Uncertainties of the Reynolds number

For the Reynolds number based on the hot-wire experiment, errors in nozzle diameter, temperature, barometric pressure were estimated at 0.04 mm, 0.7, and 1.5 %, respectively. The error resulting from the temperature loading effect was 6.1 %. The calibration errors were estimated at 1.0–10.8 %, depending on the velocity. Finally, the typical relative uncertainties of the Reynolds numbers were within 17.2 and 10.7 % for experiments with nozzle diameters of $D = 1.5$ mm and $D = 5$ mm, respectively. The evaluation was made for cases Figs. 4b and 3d from Table 1, respectively. The confidence level of the uncertainties was 95 %.

For the Reynolds number based on the theoretical evaluation, errors in nozzle diameter, the effective diameter of the diaphragm, temperature, and barometric pressure were estimated at 0.04 mm, 3.8, 0.7, and 1.5 %, respectively. The diaphragm velocity errors were estimated at 16.1 % and 6.0 % for evaluations with nozzle diameters of $D = 1.5$ mm and $D = 5$ mm, respectively. Finally, the relative uncertainties of the Reynolds numbers were within 18.3 and 10.1 % for evaluations with nozzle diameters of $D = 1.5$ mm and $D = 5$ mm, respectively. The confidence level of the uncertainties was 95 %.

For the Reynolds number based on the LDV experiment, errors in nozzle diameter, the effective diameter of the diaphragm, temperature, and barometric pressure were estimated at 0.04 mm, 3.8, 0.7, and 1.5 %, respectively. Finally, the relative uncertainties of the Reynolds numbers were within 8.7 and 7.8 % for experiments with nozzle diameters of $D = 1.5$ mm and $D = 5$ mm, respectively. The confidence level of the uncertainties was 95 %.

Uncertainties of the Stokes number

For the Stokes number evaluation, errors in nozzle diameter, temperature, and barometric pressure were estimated at 0.04 mm, 0.7, and 1.5 %, respectively. Finally, the Stokes number relative uncertainties were within 4.0 and 1.6 % for experiments with nozzle diameters of $D = 1.5$ mm and $D = 5$ mm, respectively. The confidence level of the uncertainties was 95 %.

Appendix B: Sinusoidal character of the diaphragm and SJ flow oscillations

The diaphragm surface velocity was measured using laser Doppler vibrometry (LDV). Assuming the continuity equation, incompressibility, a rigid (piston-like) diaphragm, and the slug flow model, the velocity at the orifice (u_0) was evaluated during the driven cycle—see the curve marked as "u_0, LDV evaluation" in Fig. 10. This velocity was found to be very close to the ideal sine waveform, as Fig. 10 illustrates. To quantify the very small differences, the crest factors of both curves were calculated. For the u_0 curve and for the ideal sine curve, the crest factors were 1.44 and $2^{0.5}$, respectively—i.e., the difference in both was only 1.8 %. It can be concluded that direct LDV measurement of the diaphragm velocity confirms the sinusoidal character of the diaphragm oscillations.

Unlike the sinusoidal character of the diaphragm oscillations, the velocity cycle generated by the SJ actuator can exhibit significant deviations from a sinusoidal character, resulting from the fluid dynamics during SJ formation. Namely, the flow field patterns of the extrusion and suction strokes are basically different. While the extrusion stroke generates a streamwise velocity component (and a radial entrainment component is of lesser importance), the flow field during the suction stroke assumes the characteristics of a three-dimensional (centripetal) sink. Therefore, the velocity vectors are inclined towards the axis in the off-axis regions during the suction stroke. To demonstrate these effects for the present SJ actuator, a hot-wire velocity measurement was performed at the SJ actuator orifice ($x = 0$, $r = 0$). Figure 10 shows the results as the $U + U_P$ velocity—see "$U + U_P$, CTA measurement" curve. During the extrusion stroke, the $U + U_P$ curve corresponds reasonably well with the LDV evaluation. It is worth noting here that this agreement is important for evaluation of the Reynolds number. Namely, the *Re* is based on the time-mean orifice velocity U_0, which is defined solely from the extrusion stroke—see Eq. (1).

On the other hand, there were evident differences between the curves, "$U + U_P$, CTA measurement" and "u_0, LDV evaluation", during the suction stroke. This effect demonstrates the above mentioned three-dimensional character of the suction stroke.

Another meaningful effect was an occurrence of around-zero gaps on the $U + U_P$ curve between the extrusion and suction strokes. These gaps are typical for all hot-wire measurements of SJs. They indicate that the velocity magnitude is below the low end of the hot-wire calibration range—see Smith and Glezer (1998). However, a link-up between the extrusion and suction strokes is usually a rather smooth line, occurring near the ideal sine curve. Surprisingly, Fig. 10 shows a deflecting tendency of the $U + U_P$ curve near these gaps. Apparently, this effect is linked with the present low Reynolds numbers because no similar effect was observed at a higher *Re* range—cf. SJ experiments by Trávníček et al. (2006) at $Re = 8{,}200$. An estimation of a more probable link-up over these gaps is shown by the dotted (near-sine) lines in Fig. 10. Note that this effect is negligible for evaluation of the time-mean orifice velocity U_0.

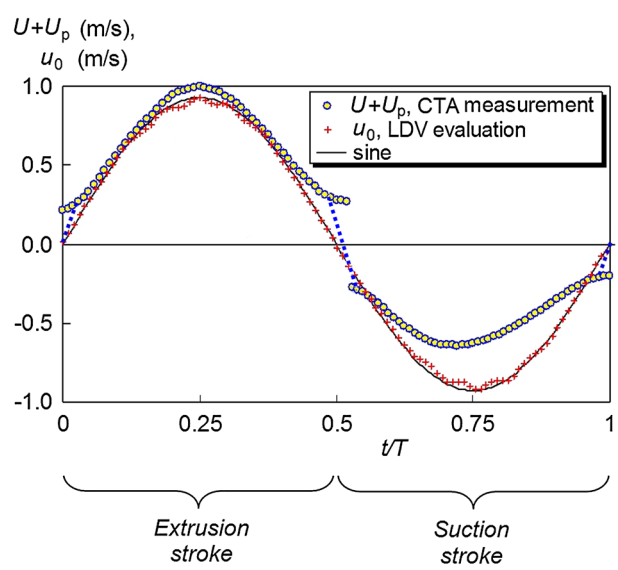

Fig. 10 Phase-locked velocity component at the SJ actuator orifice ($x = 0$, $r = 0$) for parameters of the 6b case ($D = 1.5$ mm, $f = 1.5$ mm—see parameters in Table 1)

References

Amitay M, Glezer A (2002) Controlled transients of flow reattachment over stalled airfoils. Int J Heat Fluid Fl 23:690–699

Arik M (2007) An investigation into feasibility of impingement heat transfer and acoustic abatement of meso scale synthetic jets. Appl Therm Eng 27:1483–1494

Ben Chiekh M, Bera JC, Sunyach M (2003) Synthetic jet control for flows in a diffuser: vectoring, spreading and mixing enhancement. J Turbul 4:1–12

BIPM, IEC, IFCC, IIAC, ISO, IUPAC, IUPAP, OIML (2008) Evaluation of measurement data—guide to the expression of uncertainty in measurement. Joint Committee for Guides in Metrology (JCGM 100:2008, GUM 1995 with minor corrections). http://www.bipm.org/utils/common/documents/jcgm/JCGM_100_2008_E.pdf

Cater JE, Soria J (2002) The evolution of round zero-net-mass-flux jets. J Fluid Mech 472:167–200

Chaudhari M, Puranik B, Agrawal A (2010) Heat transfer characteristics of synthetic jet impingement cooling. Int J Heat Mass Tran 53:1057–1069

Chen F-J, Beeler GB (2002) Virtual shaping of a two-dimensional NACA 0015 airfoil using synthetic jet actuator. AIAA Paper 2002-3273

Crook A, Wood NJ (2001) Measurements and visualisation of synthetic jets. AIAA Paper 2001-0145

Dauphinee TM (1957) Acoustic air pump. Ref Sci Instrum 28:456

Gallas Q, Holman R, Nishida T, Carroll B, Sheplak M, Cattafesta L (2003) Lumped element modeling of piezoelectric-driven synthetic jet actuators. AIAA J 41:240–247

Gillespie MB, Black WZ, Rinehart C, Glezer A (2006) Local convective heat transfer from a constant heat flux flat plate cooled by synthetic air jets. J Heat Transf Trans ASME 128:990–1000

Glezer A, Amitay M (2002) Synthetic jets. Annu Rev Fluid Mech 34:503–529

Goodfellow SD, Yarusevych S, Sullivan PE (2013) Smoke-wire flow visualization of a synthetic jet. J Vis 16:9–12

Holman R, Utturkar Y, Mittal R, Smith BL, Cattafesta L (2005) Formation criterion for synthetic jets. AIAA J 43:2110–2116

Hong G (2006) Effectiveness of micro synthetic jet actuator enhanced by flow instability on controlling laminar separation caused by adverse pressure gradient. Sens Actuator A Phys 132:607–615

James RD, Jacobs JW, Glezer A (1996) A round turbulent jet produced by an oscillating diaphragm. Phys Fluids 8:2484–2495

Kercher DS, Lee J-B, Brand O, Allen MG, Glezer A (2003) Microjet cooling devices for thermal management of electronics. IEEE Trans Compon Pack Manuf Technol 26:359–366

Kordík J, Trávníček Z (2013) Axisymmetric synthetic jet actuators with large streamwise dimensions. AIAA J 51(12):2862–2877

Kordík J, Broučková Z, Vít T, Pavelka M, Trávníček Z (2014) Novel methods for evaluation of the Reynolds number of synthetic jets. Exp Fluids 55:1757

Kral LD, Donovan JF, Cain AB, Cary AW (1997) Numerical simulation of synthetic jet actuators. AIAA Paper 97-1824

Lee CY, Goldstein DB (2002) Two-dimensional synthetic jet simulation. AIAA J 40:510–516

Lee A, Timchenko V, Yeoh GH, Reizes JA (2012a) Three-dimensional modelling of fluid flow and heat transfer in micro-channels with synthetic jet. Int J Heat Mass Tran 55:198–213. Erratum (2012) in Int J Heat Mass Tran 55:2746

Lee A, Yeoh GH, Timchenko V, Reizes JA (2012b) Flow structure generated by two synthetic jets in a channel: effect of phase and frequency. Sens Actuator A Phys 184:98–111

Mahalingam R, Rumigny N, Glezer A (2004) Thermal management using synthetic jet ejectors. IEEE Trans Compon Packag Technol 27:439–444

Mallinson SG, Reizes A, Hong G (2001) An experimental and numerical study of synthetic jet flow. Aeronaut J 105:41–49

McGuinn A, Farrelly R, Persoons T, Murray DB (2013) Flow regime characterisation of an impinging axisymmetric synthetic jet. Exp Therm Fluid Sci 47:241–251

Meier HU, Zhou M-D (1991) The development of acoustic generators and their application as a boundary-layer-transition control device. Exp Fluids 11:93–104

Milanovic IM, Zaman KBMQ (2005) Synthetic jets in crossflow. AIAA J 43:929–940

Mittal R, Rampunggoon P (2002) On the virtual aeroshaping effect of synthetic jets. Phys Fluids 14:1533–1536

Ng I, Timchenko V, Reizes J, Trávníček Z, Kordík J, Broučková Z (2013) Synthetic jets at low Stokes number: numerical and experimental approach. In: Tenth International Conference on Flow Dynamics OS7-8:472–473, Sendai

Pack LG, Seifert A (2001) Periodic excitation for jet vectoring and enhanced spreading. J Aircraft 38:486–495

Persoons T, McGuinn A, Murray DB (2011) A general correlation for the stagnation point Nusselt number of an axisymmetric impinging synthetic jet. Int J Heat Mass Tran 54:3900–3908

Shuster JM, Smith DR (2007) Experimental study of the formation and scaling of a round synthetic jet. Phys Fluids 19:045109

Smith BL, Glezer A (1998) The formation and evolution of synthetic jets. Phys Fluids 10:2281–2297

Smith BL, Glezer A (2002) Jet vectoring using synthetic jets. J Fluid Mech 458:1–34

Smith BL, Swift GW (2003) A comparison between synthetic jets and continuous jets. Exp Fluids 34:467–472

Tamburello DA, Amitay M (2007) Three-dimensional interactions of a free jet with a perpendicular synthetic jet. J Turbul 8:1–18

Tensi J, Boué I, Paillé F, Dury G (2002) Modification of the wake behind a circular cylinder by using synthetic jets. J Vis 5:37–44

Timchenko V, Reizes J, Leonardi E, de Vahl Davis G (2004) A criterion for the formation of micro synthetic jets. In: Proceedings of IMECE04, IMECE2004-61374 260:197–203, New York

Timchenko V, Reizes JA, Leonardi E (2007) An evaluation of synthetic jets for heat transfer enhancement in air cooled micro-channels. Int J Numer Methods Heat Fluid Flow 17:263–283

Trávníček Z, Tesař V (2003) Annular synthetic jet used for impinging flow mass-transfer. Int J Heat Mass Tran 46:3291–3297

Trávníček Z, Vít T, Tesař V (2006) Hybrid synthetic jets as the non-zero-net-mass-flux synthetic jets. Phys Fluids 18:081701

Trávníček Z, Broučková Z, Kordík J (2012a) Formation criterion for axisymmetric synthetic jets at high Stokes numbers. AIAA J 50(9):2012–2017

Trávníček Z, Němcová L, Kordík J, Tesař V, Kopecký V (2012b) Axisymmetric impinging jet excited by a synthetic jet system. Int J Heat Mass Tran 55:1279–1290

Trávníček Z, Dančová P, Kordík J, Vít T, Pavelka M (2012c) Heat and mass transfer caused by a laminar channel flow equipped with a synthetic jet array. Trans ASME J Thermal Sci Eng Appl 2:041006-1–041006-8

Trávníček Z, Broučková Z, Kordík J (2013) Visualization of synthetic jet formation in air. In: 12th International Symposium on Fluid Control, Measurement and Visualization FLUCOME2013 OS6-02-2, Nara

Valiorgue P, Persoons T, McGuinn A, Murray DB (2009) Heat transfer mechanisms in an impinging synthetic jet for a small jet-to-surface spacing. Exp Therm Fluid Sci 33:597–603

Watson GMG, Sigurdson LW (2008) The controlled relaminarization of low velocity ratio elevated jets-in-crossflow. Phys Fluids 20:094108

Xia Q, Zhong S (2012a) An experimental study on the behaviours of circular synthetic jets at low Reynolds numbers. Proc Inst Mech Eng Part C J Eng Mech Eng Sci 226:2686–2700

Xia Q, Zhong S (2012b) A PLIF and PIV study of liquid mixing enhanced by a lateral synthetic jet pair. Int J Heat Fluid Flow 37:64–73

Xia Q, Lei S, Ma J, Zhong S (2014) Numerical study of circular synthetic jets at low Reynolds numbers. Int J Heat Fluid Flow 50:456–466

Yassour Y, Stricker J, Wolfshtein M (1986) Heat transfer from a small pulsating jet. In: Proceedings of 8th International Heat Transfer Conference 3:1183–1186, San Francisco

Yehoshua T, Seifert A (2006) Boundary condition effects on the evolution of a train of vortex pairs in still air. Aeronaut J 110:397–417

Zhou J, Tang H, Zhong S (2009) Vortex roll-up criterion for synthetic jets. AIAA J 47:1252–1262